

<https://doi.org/10.1038/s43246-024-00605-1>

Sharp-peaked lanthanide nanocrystals for near-infrared photoacoustic multiplexed differential imaging

Check for updates

Kang Yong Loh^{1,2,3,16}, Lei S. Li^{4,5,16}, Jingyue Fan^{6,16}, Yi Yiing Goh^{6,7}, Weng Heng Liew¹, Samuel Davis⁴, Yide Zhang⁴, Kai Li^{1,8}, Jie Liu⁹, Liangliang Liang⁶, Minjun Feng¹⁰, Ming Yang¹¹, Hang Zhang¹¹, Ping'an Ma¹², Guangxue Feng¹³, Zhao Mu¹⁰, Weibo Gao^{10,14}, Tze Chien Sum¹⁰, Bin Liu¹³, Jun Lin¹², Kui Yao¹, Lihong V. Wang⁴ ✉ & Xiaogang Liu^{1,6,15} ✉

Photoacoustic tomography offers a powerful tool to visualize biologically relevant molecules and understand processes within living systems at high resolution in deep tissue, facilitated by the conversion of incident photons into low-scattering acoustic waves through non-radiative relaxation. Although current endogenous and exogenous photoacoustic contrast agents effectively enable molecular imaging within deep tissues, their broad absorption spectra in the visible to near-infrared (NIR) range limit photoacoustic multiplexed imaging. Here, we exploit the distinct ultrasharp NIR absorption peaks of lanthanides to engineer a series of NIR photoacoustic nanocrystals. This engineering involves precise host and dopant material composition, yielding nanocrystals with sharply peaked photoacoustic absorption spectra (~3.2 nm width) and a ~10-fold enhancement in NIR optical absorption for efficient deep tissue imaging. By combining photoacoustic tomography with these engineered nanocrystals, we demonstrate photoacoustic multiplexed differential imaging with substantially decreased background signals and enhanced precision and contrast.

Photoacoustic tomography (PAT) that capitalizes on the photoacoustic (PA) effect is a powerful technique for biological research and medical diagnosis. It combines the advantages of high optical contrast from light-matter interactions with high spatial resolution from ultrasound detection, enabling molecular-level imaging within deep biological tissues¹⁻³. While PA imaging provides contrast at all scales, ranging from organelles⁴⁻⁸ and cells⁹⁻¹¹ to whole bodies of small animals^{12,13} and human organs¹⁴⁻¹⁶, its true strength lies in its ability to deliver high-resolution

images of deep tissue and molecular contrast, which other modalities often struggle to achieve. Conventional optical imaging, for instance, is limited in terms of penetration depth². On the other hand, methods such as magnetic resonance imaging, X-ray computed tomography, and ultrasound can provide deep tissue penetration but lack the ability to distinguish molecular contrasts effectively¹⁷⁻¹⁹.

PAT overcomes these limitations by leveraging interactions between light and matters. Both endogenous and exogenous PA

¹Institute of Materials Research and Engineering, Agency for Science, Technology and Research (A*STAR), Singapore, Singapore. ²Department of Chemistry, Stanford University, Stanford, CA, USA. ³Sarafan ChEM-H, Stanford University, Stanford, CA, USA. ⁴Caltech Optical Imaging Laboratory, Andrew and Peggy Cherng Department of Medical Engineering, Department of Electrical Engineering, California Institute of Technology, Pasadena, CA, USA. ⁵Department of Electrical and Computer Engineering, Rice University, Houston, TX, USA. ⁶Department of Chemistry, National University of Singapore, Singapore, Singapore. ⁷NUS Graduate School, National University of Singapore, Singapore, Singapore. ⁸Shenzhen Key Laboratory of Smart Healthcare Engineering, Department of Biomedical Engineering, Southern University of Science and Technology, Shenzhen, China. ⁹Key Laboratory of Flexible Electronics (KLOFE), Institute of Advanced Materials (IAM), Nanjing Tech University, Nanjing, China. ¹⁰Division of Physics and Applied Physics, School of Physical and Mathematical Sciences, Nanyang Technological University, Singapore, Singapore. ¹¹Institute of Engineering Thermophysics, Chinese Academy of Sciences, Beijing, China. ¹²State Key Laboratory of Rare Earth Resource Utilization, Changchun Institute of Applied Chemistry, Chinese Academy of Sciences, Changchun, China. ¹³Department of Chemical and Biomolecular Engineering, National University of Singapore, Singapore, Singapore. ¹⁴The Photonics Institute and Centre for Disruptive Photonic Technologies, Nanyang Technological University, Singapore, Singapore. ¹⁵Nanomedicine Translational Research Programme, Centre for NanoMedicine, Yong Loo Lin School of Medicine, National University of Singapore, Singapore, Singapore. ¹⁶These authors contributed equally: Kang Yong Loh, Lei S. Li, Jingyue Fan. ✉ e-mail: Lvw@caltech.edu; chmlx@nus.edu.sg

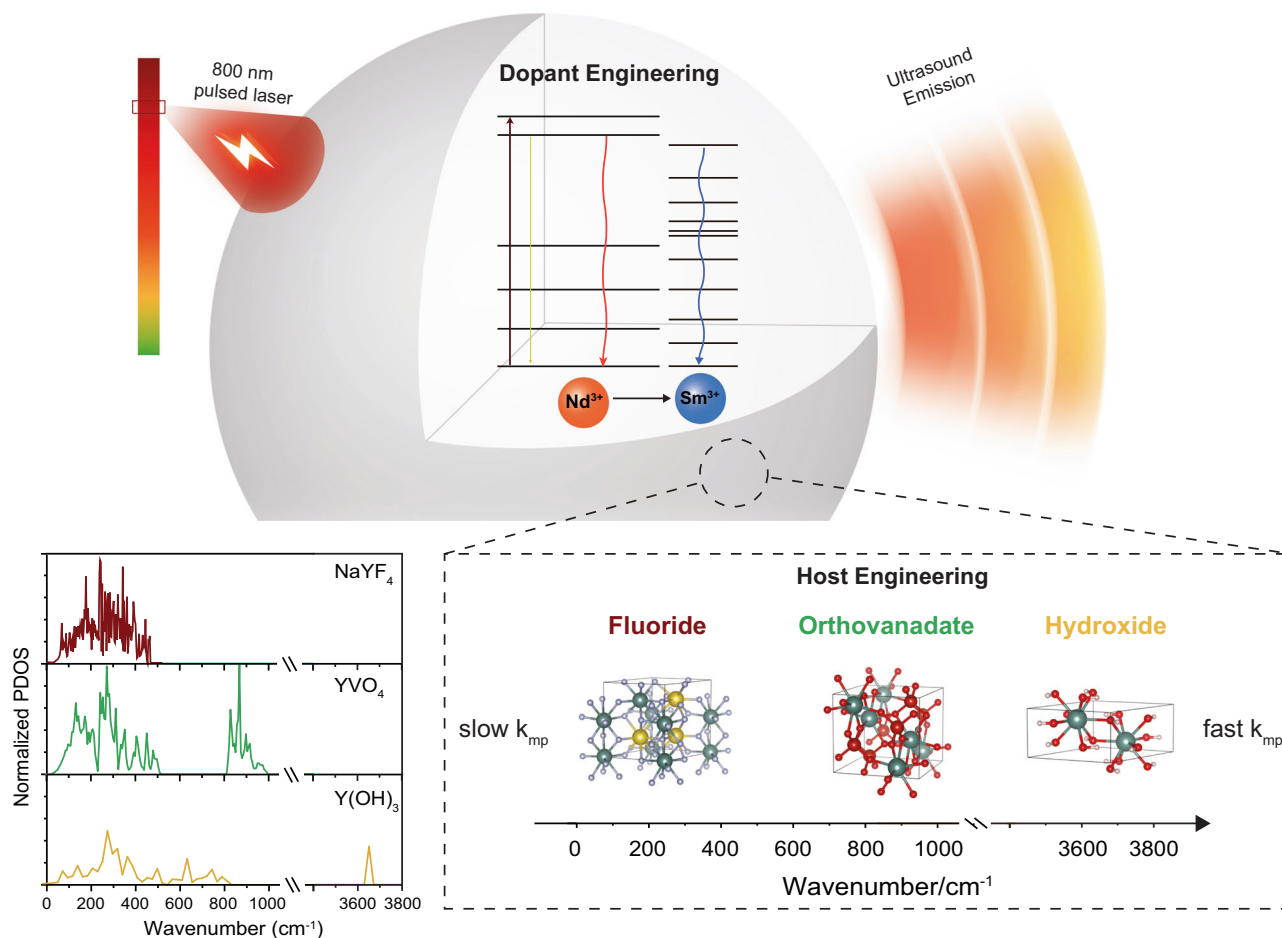


Fig. 1 | Near-infrared photoacoustic multiplexed differential imaging (NIR-PAMDI) through the use of sharp-peaked lanthanide nanocrystals. Photoexcitation of Nd^{3+} phonon sensitizers in nanocrystal host lattices enables efficient photon absorption and PA generation. The presence of Nd^{3+} in high concentration quenches excitation energy and prevents photon emission through non-radiative cross-relaxation. This non-radiative decay pathway can be further enhanced by energy transfer to Sm^{3+} dopants, whose dense energy states match the intermediate energy level $^4\text{F}_{2/3}$ of long-lifetime Nd^{3+} . Based on first principles phonon density of states (PDOS) calculations, we hypothesize that host lattices with higher phonon

energies exhibit higher multiphonon relaxation rates (k_{mp}), which promote non-radiative relaxation, leading to more pronounced phonon cascade events. Manipulating the host material from fluoride (with a slow multiphonon relaxation rate, k_{mp}) to orthovanadate and hydroxide (with faster k_{mp}) facilitates stronger host-lattice vibrations, further promoting non-radiative energy dissipation from excited ions. The increase in non-radiative decay of energy states consequently induces thermal expansion at sharp wavelengths.

contrast agents use organic and inorganic molecules to transduce photons to phonons^{4,20–25}. However, a significant challenge arises from the broad absorption spectra exhibited by current contrast agents. These absorption peaks are typically wide, with a full width at half maximum (FWHM) ranging from 50 nm to 200 nm. These broad peaks lead to substantial spectral overlaps in PA signals, making it challenging to conduct PA multiplexed imaging in deep tissue. Therefore, it is essential to engineer PA agents with sharp absorption peaks in the near-infrared (NIR) wavelength range to enable deep-tissue multiplexed imaging⁴.

Herein, we report the development of nanocrystals that enhance phonon generation and exhibit sharply peaked absorption in the NIR region. Lanthanide elements have distinctively different photophysical properties from other elements, thanks to their 4f-4f electronic transitions. Only photons with specific energy and wavelengths to excite ground-state electrons with unique energy absorption pathways during photoexcitation can occur. The sharp absorption peaks are mainly attributed to the effective shielding effects of the 4f electron orbitals by the 5s and 5p subshells. Hence, there is little linewidth broadening from neighboring crystal ligand field interactions (Fig. 1). Previous attempts to develop lanthanide-doped particles for PAT have either relied on upconversion luminescence^{21,22} to excite

molecular dyes for photothermal effects or employed surface quenching mechanisms^{23,24} to induce PA effects. These strategies resulted in agents with broadband absorption characteristics due to dye conjugation or weak PA emission as a result of limited thermal generation with surface quenching. We demonstrate that by engineering the host lattice of nanocrystals and the dopant elements, sharp optical absorption peaks associated with these stringent 4f-4f energy transitions can be enhanced.

Results and discussion

Nd^{3+} -doped nanocrystals exhibit sharp PA spectra

Neodymium (Nd^{3+}) was selected as the phonon sensitizer due to its sharp NIR absorption peak near 800 nm^{25–28}, which is optimal for deep tissue penetration in biological tissues. Lanthanide ions, including Nd^{3+} , are susceptible to cross-relaxation and non-radiative processes, particularly when numerous excited Nd^{3+} states are present in nanocrystals. This can lead to a loss of excitation energy and prevent photon emission^{27,28}. Moreover, the closely spaced energy gaps in the Nd^{3+} 4f electronic structure make its $^4\text{F}_{5/2}$ emission state extremely prone to cross-relaxation at a short interionic distance and heat generation at high doping concentrations^{29,30}. While this property is undesirable for photoluminescence, it is ideal for generating PA waves, where phonon generation is preferred over photon emission. In

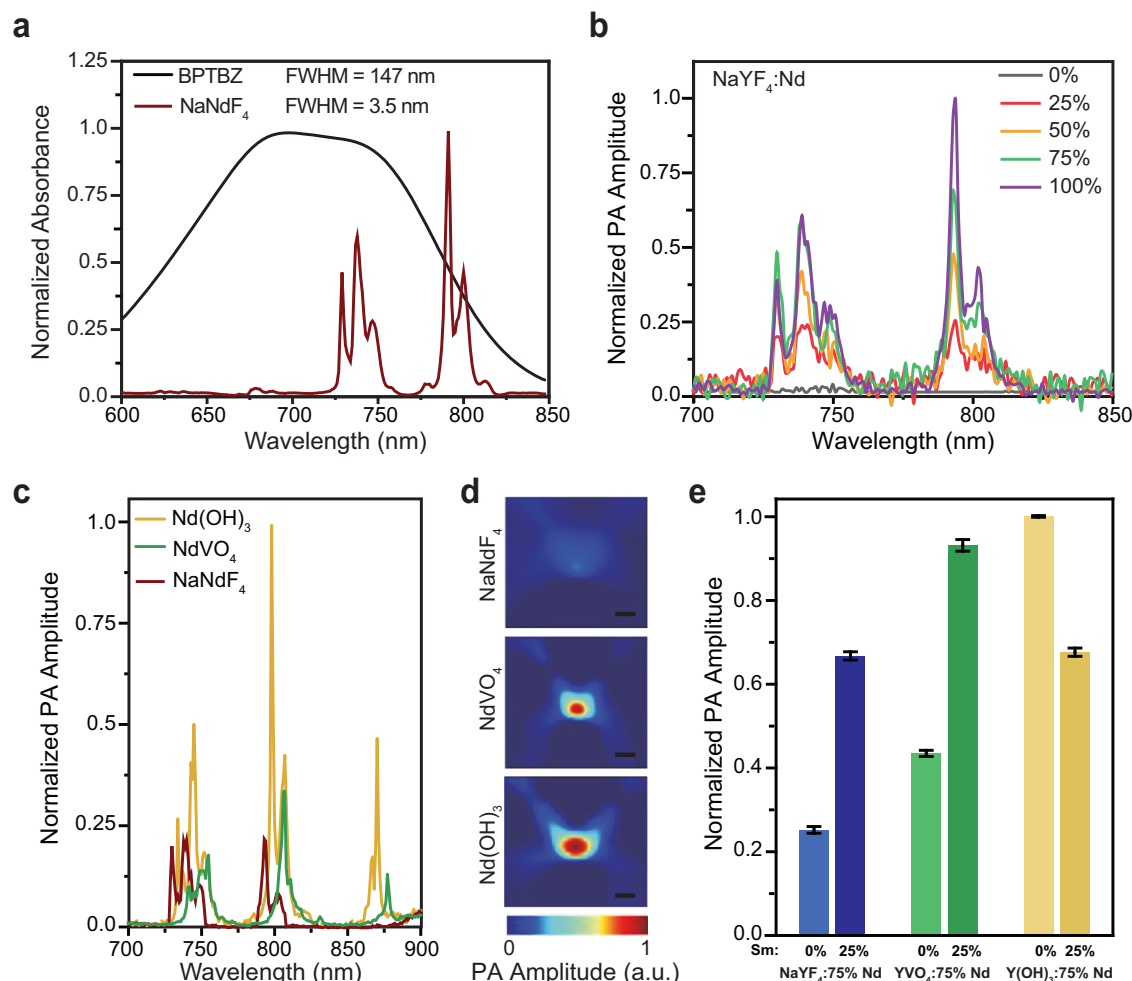


Fig. 2 | Non-radiative relaxation pathways in Nd³⁺-doped lanthanide nanocrystals and enhanced PA spectra. **a** Absorption spectrum revealing the significantly sharper absorption profile of polyvinylpyrrolidone (PVP)-coated NaNdF₄ nanocrystals (NaNdF₄@PVP) compared with broadly absorbing polymeric BPTBZ nanoparticles. **b** PA spectra of Nd³⁺-doped NaYF₄@PVP nanocrystals, showing a positive correlation between PA amplitude and Nd³⁺ doping concentration. **c** PA

spectra of NaNdF₄@PVP, NdVO₄@PVP, and Nd(OH)₃@PVP nanocrystals, demonstrating the effect of host selection on PA amplitude. **d** In vitro PA imaging of NaNdF₄@PVP, NdVO₄@PVP, and Nd(OH)₃@PVP. (Scale bar: 1 mm) **e** PA signals recorded for various types of nanocrystals at different Sm³⁺ dopant concentrations. The error bars denote the sample standard deviations.

contrast, conventional PA agents, despite having a high extinction coefficient, have broad absorption profiles due to their π -conjugated system or plasmonic resonance. The choice of nanocrystal host lattice also influences photon generation and, consequentially, phonon processes. Heavy halides like chlorides, bromides, and iodides have low phonon energies, while oxides exhibit higher phonon energies due to lattice vibrations (500 cm⁻¹ and above)³¹. The selection of halides and oxides as host materials can further expedite the non-radiative relaxation of excited Nd³⁺ ions through multiphonon relaxation^{32,33}.

Considering these principles, we chose heavily doped fluoride nanoparticle as the PA probe. Optical absorption measurements of NaNdF₄ nanocrystals (Supplementary Figs. 1, 2 and Supplementary Table 1) revealed a sharp NIR absorption peak with a narrow FWHM of ~3.5 nm at 794 nm, corresponding to a strict $4f-4f$ energy transition state. In comparison, a polymeric PA contrast agent (BPTBZ dye) showed a typical molecular dye absorption peak with a much broader FWHM of ~147 nm (Fig. 2a and Supplementary Fig. 3). Increasing the phonon sensitizer Nd³⁺ dopant within the fluoride lattice systematically increased absorbance and introduced additional non-radiative pathways, resulting in higher PA amplitude while preserving sharp peak characteristics (Fig. 2b and Supplementary Figs. 4, 5).

Enhancing NIR phonon generation through host and dopant engineering

In a fluoride host lattice, the presence of a weak optical phonon mode with frequencies from 300 to 350 cm⁻¹ leads to a slower multiphoton relaxation process and relatively lower amplitudes in PA signals. On the other hand, an orthovanadate (VO₄) host lattice exhibits an intermediate optical phonon mode at ~1000 cm⁻¹. In contrast, the hydroxide (OH) host lattice stands out due to its possession of six extremely high-frequency phonon modes, each vibrating at ~3600 cm⁻¹. These elevated frequencies arise from the stretching of O-H bonds (Supplementary Figs. 6 and 7). Notably, these high-frequency phonon modes play a pivotal role in promoting non-radiative decay processes and, as a result, facilitate the rapid generation of phonons. Our rationale led us to explore the possibility of engineering host lattices with progressively higher phonon modes, with the aim of facilitating faster and more efficient non-radiative decay pathways from excited Nd³⁺ ions residing within the crystal lattice (Fig. 2c). Our experiments demonstrated a direct relationship between the host lattice's phonon energy and the resulting PA amplitudes. Specifically, as we transitioned from fluoride (F) to VO₄ to OH host lattices (Supplementary Figs. 1, 8, 9 and Supplementary Tables 2, 3), each characterized by increasing phonon energies, we observed a systematic increase in the net PA amplitude (Fig. 2c). OH host lattices

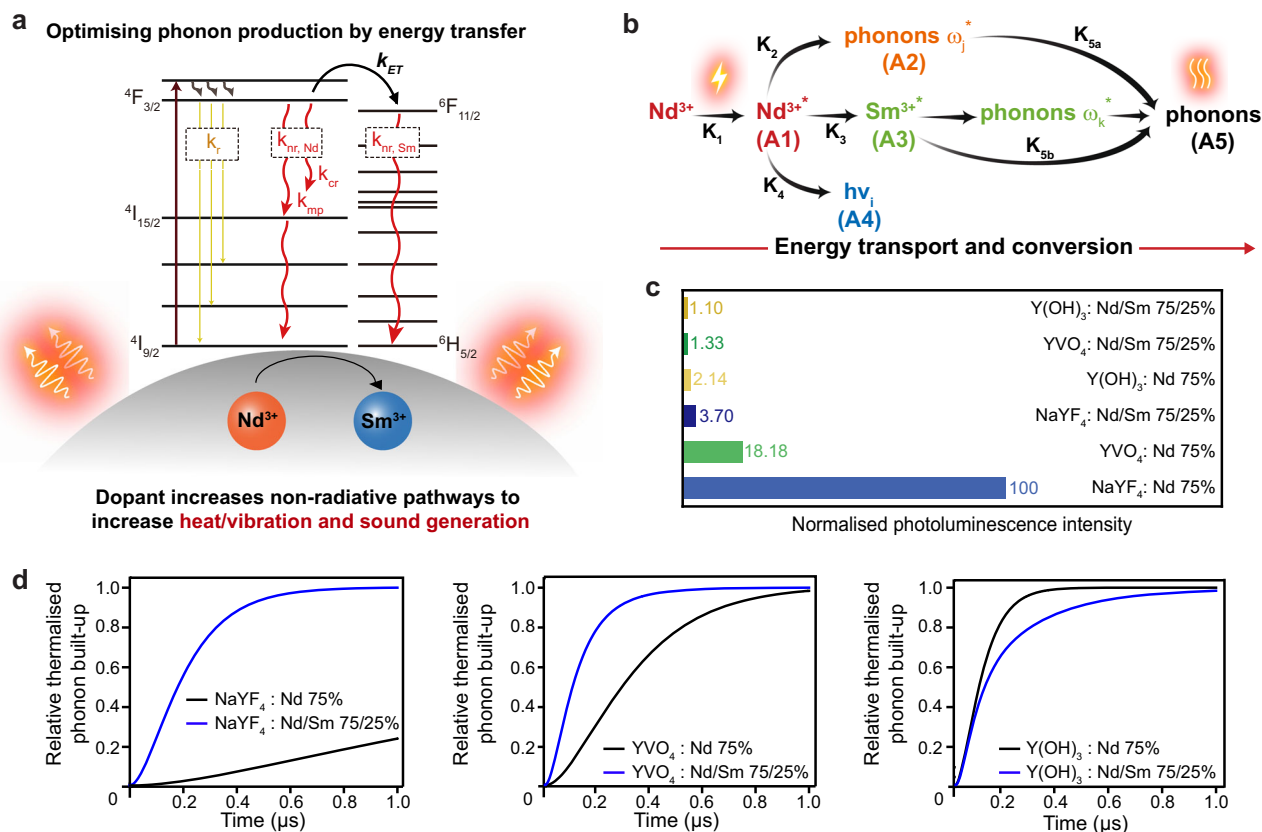


Fig. 3 | Proposed phonon engineering mechanism for lanthanide nanocrystals. **a** Schematic depicting the distribution of electronic energy levels for active lanthanide dopant ions. Excited neodymium follows non-radiative decay pathways in a host lattice. **b** Proposed energy conversion and relaxation pathways from an excited Nd^{3+} ion. The asterisks denote excited states. K_1 denotes the absorption coefficient of the ground state of Nd^{3+} ; K_2 denotes the nonradiative relaxation rate constant in the excited Nd^{3+} ; K_3 denotes the energy transfer rate constant from an excited Nd^{3+} to a

ground state of Sm^{3+} ; K_4 denotes the radiative decay constant in the excited Nd^{3+} ; K_{5a} denotes the equilibration of excited phonons; K_{5b} denotes the nonradiative relaxation rate constant from an excited Sm^{3+} . **c** Normalized photoluminescence intensity of PA contrast agents based on lanthanide doping with various host and dopant compositions. **d** Calculated kinetics of thermalized phonon built-up influenced by host and dopant compositions.

produced PA signals three times higher than F hosts and two times higher than VO_4 hosts. This host-dependent variation in PA performance can be attributed to differences in the rates of multiphonon relaxation of excited Nd^{3+} ions (Supplementary Note 1). In vitro PA imaging further confirms this trend, showing increasing PA amplitude with higher host lattice phonon energies (Fig. 2d). Intriguingly, the introduction of Sm^{3+} dopants in OH hosts results in a 30% decrease in PA signals, despite a twofold reduction in photoluminescence (Fig. 2e and Supplementary Figs. 10–12). This phenomenon could be attributed to a slower non-radiative rate via Sm^{3+} following energy transfer from Nd^{3+} compared to the non-radiative rate directly from Nd^{3+} in the OH host. It suggests that additional dopants within OH hosts might redirect non-radiative pathways away from the high phonon mode host lattices. These findings indicate that co-doping Sm^{3+} alongside phonon sensitizers within host lattices reduces overall photoluminescence in nanocrystals while providing additional non-radiative decay channels that enhance PA generation.

Mechanistic investigations

Phonon production within lanthanide-doped nanoparticles is a key factor that can be engineered through host lattice manipulation and energy transfer to co-dopant ions, ultimately governing the generation of PA signals (Fig. 3a). When an Nd^{3+} ion becomes excited, it has two primary pathways for non-radiation to the ground state. It can either couple with the vibrational modes of the host lattice, denoted as k_2 , or transfer its energy to a neighboring Sm^{3+} co-dopant with denser electronic levels, represented as k_3 (Fig. 3b). Therefore, the difference in PA signal generation observed across

different hosts can be attributed to differences in k_2 . For example, hydroxide lattices exhibit high-energy vibrational modes, including six O–H stretching modes (Supplementary Figs. 6 and 7), which significantly increase the value k_2 in $\text{Y(OH)}_3:\text{Nd}(75\%)$ nanoparticles. Conversely, fluoride host lattices primarily feature lower frequency phonon modes, reducing the value of k_2 in $\text{NaYF}_4:\text{Nd}(75\%)$ nanoparticles. The disparities in k_2 were confirmed through PL measurements, which exhibited an inversely proportional relationship with k_2 .

We systematically investigated the PL and PA effects of host lattices (F, VO_4 , and OH) while maintaining a constant 75% Nd^{3+} phonon sensitizer concentration (Supplementary Figs. 11–13). The results revealed that lanthanide-doped nanocrystals with enhanced phonon modes exhibited lower PL intensities. Specifically, F host lattices exhibited the highest photoluminescence intensities, while OH host lattices exhibited the lowest photon emission (Fig. 3c). This decrease in PL serves as evidence of reduced radiative decay and an increase in non-radiative pathways leading to phonon generation. Furthermore, PA signal intensity has been shown to correlate with the rate of heat generation^{34,35}. In our study, we modeled PA signal generation using coupled kinetics rate equations (Fig. 3b and Supplementary Note 2). The increased production rate of thermalized phonons correlates with greater PA signal. $\text{Y(OH)}_3:\text{Nd}(75\%)$ was estimated to have a much higher non-radiative decay rate constant than $\text{YVO}_4:\text{Nd}(75\%)$ or $\text{NaYF}_4:\text{Nd}(75\%)$ ($20,160 \text{ ms}^{-1}$ vs. 5400 ms^{-1} vs. 420 ms^{-1}) (Supplementary Note 2). Therefore, one crucial factor contributing to the substantial increase in PA amplitude is the accelerated production of thermally excited phonons (Fig. 3d).

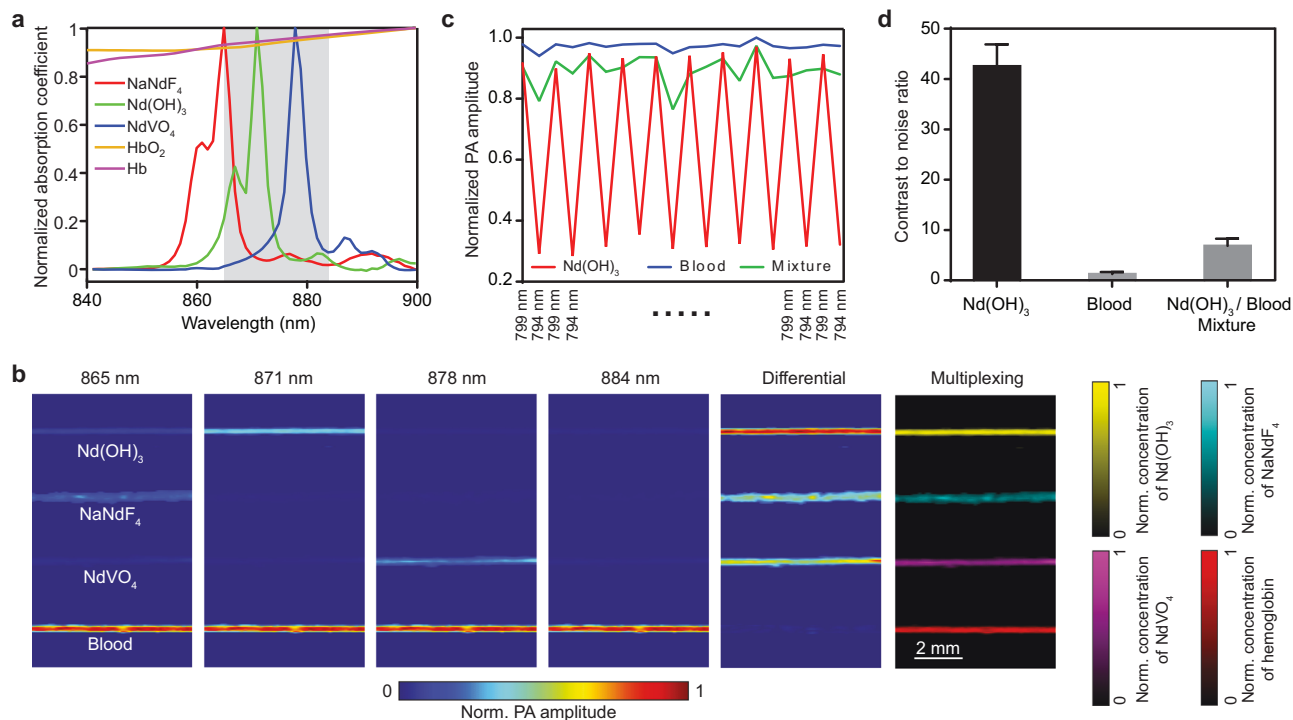


Fig. 4 | Near-infrared photoacoustic multiplexed differential imaging (NIR-PAMDi). **a** Normalized absorption spectra of NaNdF₄:Nd/Sm(75/25%), NdVO₄:Nd/Sm(75/25%), Nd(OH)₃, oxy-hemoglobin, and deoxy-hemoglobin. Phonon-enhanced lanthanide nanocrystals display distinct sharp peaks compared with the broader absorption files of endogenous chromophores. Note that NaNdF₄:Nd/Sm(75/25%) and NdVO₄:Nd/Sm(75/25%) are annotated as NaNdF₄ and NdVO₄. **b** Multiplexed PA imaging of tubes filled with phonon-enhanced lanthanide nanocrystals and blood. Columns 1–4 show PA images excited at 865 nm, 871 nm, 878 nm, and 884 nm, respectively. Column 5 shows the differential image, $I_{diff} = (I_{865} - I_{884}) + (I_{871} - I_{884}) + (I_{878} - I_{884})$, where I_{865} , I_{871} , I_{878} , and I_{884} are PA images acquired at 865 nm, 871 nm, 878 nm, and

884 nm, respectively. Column 6 shows multiplexed PA images after linear unmixing, indicating the normalized concentrations of phonon-enhanced lanthanide nanocrystals and hemoglobin. Oxy- and deoxy-hemoglobin are combined due to their similar absorption coefficients at the excitation wavelengths. NaNdF₄:Nd/Sm(75/25%) and NdVO₄:Nd/Sm(75/25%) are annotated as NaNdF₄ and NdVO₄. “Norm.” refers to normalized. **c** PA signals of Nd(OH)₃, blood, and a 10:1 mixture of the two at alternating excitation wavelengths of 799 nm and 795 nm. Amplitude changes in Nd(OH)₃ are attributed to the large absorption difference between the two wavelengths. **d** Contrast-to-noise ratio of the differential images of Nd(OH)₃, blood, and the mixture. Bar graphs show the mean and standard deviation (s.d.).

Enhancing phonon generation for PA multiplexed imaging

The alternation of host lattices leads to changes in both the field strength and the crystallographic point group of the active dopant Nd ions, resulting in varying numbers of Stark lines and unique, sharp PA spectra for each host crystal configuration³⁶. In our pursuit of enhancing PA signals in F and VO₄ host lattices, we introduced an additional dopant, samarium, Sm³⁺. Sm³⁺ was chosen due to its densely packed energy states between ⁶F_{11/2} and ⁶H_{5/2} energy states, which have a comparable energy gap to the ⁴I_{9/2} to ⁴F_{3/2} energy excitation pathway of Nd³⁺. Our rationale was that doping Sm³⁺ into a host lattice containing Nd³⁺ phonon sensitizers would facilitate energy transfer from the excited ⁴F_{3/2} state of Nd³⁺ to the ⁶F_{11/2} state of Sm³⁺ dopants. This utilization of the dense energy states in Sm³⁺ would encourage non-radiative decay pathways. We prepared two dopant compositions for each of these two host nanocrystals: NaYF₄:Nd(75%) vs. NaNdF₄:Nd/Sm(75/25%) and YVO₄:Nd(75%) vs. NdVO₄:Nd/Sm(75/25%) (Supplementary Figs. 10–13). The introduction of 25% Sm³⁺ into hosts containing Nd³⁺ doubled the PA amplitudes in both Y and VO₄ host lattices (Fig. 2e).

We next conducted NIR photoacoustic multiplexed differential imaging (NIR-PAMDi) using these phonon-enhanced nanocrystals. NaNdF₄:Nd/Sm(75/25%), NdVO₄:Nd/Sm(75/25%), and Nd(OH)₃ exhibited much sharper absorption peaks than hemoglobin (Fig. 4a), allowing for linear unmixing within a narrow wavelength range (Supplementary Fig. 14 and Methods). The condition numbers for unmixing phonon-enhanced lanthanide-doped nanocrystals with sharp absorption peaks are about two orders of magnitude smaller than those for unmixing the organic chromophores with broad absorption spectrum (Supplementary Fig. 14 and Methods). We mixed the three phonon-enhanced nanocrystals separately

with whole blood and imaged the three mixtures together with a whole blood sample in silicone tubes within a single frame at four wavelengths: 865 nm, 871 nm, 878 nm, and 884 nm (Fig. 4b). Each nanocrystal composition could be clearly distinguished in the images at their respective peak excitation wavelengths of 865 nm, 871 nm, and 878 nm. Given that within our illumination wavelength range of 865–884 nm, the absorption coefficients for oxy- and deoxy-hemoglobin (HbO₂ and HbR) are almost identical, we treated blood as a single-contrast agent, which displayed clear visibility across all four images. Because of sharp absorption peaks, the differential image accentuated signals from the three types of nanocrystals while minimizing the interference from blood. Using linear unmixing, we achieved multiplexed PA imaging of four different contrasts. We further conducted experiments with Nd(OH)₃ mixed with blood. By alternating the illumination wavelengths between 794 nm and 799 nm (Fig. 4c and Supplementary Fig. 15a), we would distinctly observe signal changes from Nd(OH)₃ and the mixture (volume ratio blood to Nd(OH)₃, 10:1). Utilizing NIR-PAMDi, wherein we subtracted PA signals at the wavelength just 5 nm away (794 nm) from PA signals at the peak wavelength (799 nm), we enhanced the contrast-to-noise ratio by ~40-fold and visualized phonon-enhanced nanocrystals and the mixture (Fig. 4d). Moreover, we demonstrated that Nd(OH)₃ can be imaged at depths of up to 12 mm inside chicken breast tissue (Supplementary Fig. 15b), proving its capability for in vivo applications.

In vivo differential PAT

We next evaluated phonon-enhanced nanocrystals as a PA contrast agent both in vitro and in vivo, and toxicity assessments of polyvinylpyrrolidone

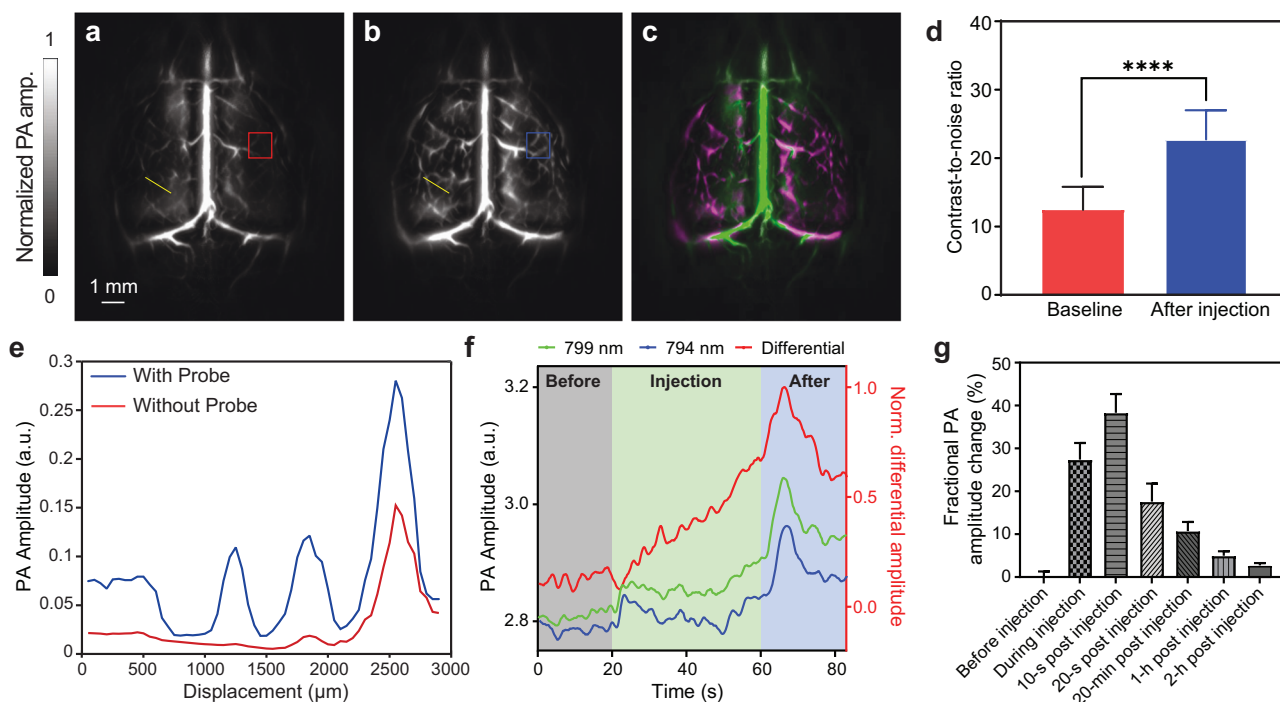


Fig. 5 | In vivo PA imaging of mouse brain vasculature. **a** Baseline PA image at 799 nm of the mouse brain, using hemoglobin as the contrast agent. **b** Differential PA image of the mouse brain acquired between 799 nm and 794 nm after injection of Nd(OH)₃ nanocrystals, using both hemoglobin and lanthanide-doped nanocrystals as contrast agents, revealing more detailed vasculature. **c** Overlaid image of the mouse brain after linear unmixing. Green represents hemoglobin contrast and magenta represents the lanthanide nanocrystal contrast. **d** Contrast-to-noise ratio

plotted before and after Nd(OH)₃ injection. **e** Line profiles along the yellow lines in **a** and **b**, illustrating the improved visibility of cortical vessels due to Nd(OH)₃ injection. **f** Time course of PA amplitude at 794 nm and 799 nm, along with the normalized differential signal, before, during, and after injection of Nd(OH)₃. **g** Fractional PA amplitude change (799 nm) throughout the experiments. Bar graphs represent the respective mean and standard deviation (s.d.).

(PVP)-coated nanocrystals (Nd(OH)₃ and NdVO₄) revealed good biocompatibility (Supplementary Fig. 16). The cell viability of U-87MG cells exposed to increasing mass concentrations of NdVO₄ and Nd(OH)₃ remained comparable to that of untreated U-87MG control cells, indicating the non-cytotoxic nature of these nanocrystals in nanoparticle form. Mice models used as control subjects, whether subjected to intravenous or intratumoral injections, maintained stable body mass over a span of 20 days.

Given the superior performance in PA imaging, we opted to employ Nd(OH)₃ nanocrystals for in vivo PA experiments (Fig. 5). Moreover, Nd(OH)₃ demonstrated PA amplitudes surpassing those of previously reported upconversion nanoprobe (Supplementary Fig. 17). To enable NIR-PAMDi, PA images were captured sequentially at 789 nm, 794 nm, and 799 nm, at a rate of 100 Hz. Consequently, the effective frame rate for multiplexed imaging reached 33.3 Hz. Initially, a baseline image of the mouse cortical vasculature was acquired at 799 nm (Fig. 5a). Subsequently, Nd(OH)₃ nanoparticles were intravenously injected during imaging, leading to an evident enhancement in the contrast of small cortical vessels within the 799 nm image. To enhance the visualization of the enhancement from Nd(OH)₃, we overlaid the differential image between 799 nm and 794 nm onto the original 799 nm image (Fig. 5b). Utilizing just three narrow-wavelength ranges (789 nm, 794 nm, and 799 nm), we effectively distinguished PA signals originating from Nd(OH)₃, HbO₂, and HbR, facilitated by the distinctive absorption peaks of Nd(OH)₃. The PA signals from Nd(OH)₃, depicted in magenta after linear unmixing, intensified the contrast and visibility of cortical vessels by a factor of two (Fig. 5c–e). We also plotted the changes in PA signal amplitudes at 794 nm and 799 nm, along with their differential amplitude over the course of the experiment (Fig. 5f). The PA signals peaked at 10 seconds post-injection and gradually returned to baseline levels over two hours, indicative of the efficient clearance of Nd(OH)₃ (Fig. 5g).

Conclusions

The utilization of lanthanide-doped nanocrystals represents a promising avenue for advancing NIR PA contrast agents by harnessing the unique *f-f* transition properties of lanthanide elements. We have shown that it is possible to improve absorption cross-sections and PA signals through dopant and host engineering. In future iterations of lanthanide-doped PA contrast agents, there is an opportunity to explore a wide range of host materials that could further enhance the PA signals or alternative doping strategies that promote non-radiative relaxation in lanthanide-doped nanocrystals, particularly by utilizing host materials with low quantum yields.

Furthermore, phonon-enhanced lanthanide-doped nanocrystals are well-suited for PA multiplexed imaging due to the unique sharp absorption peaks and offer the possibility of reporting disease states in living systems. Functional modifications, such as the attachment of antibodies or ligands, enable targeting of specific cell surface receptors, providing information about the functional status of tissues in physiological systems. Moreover, these probes possess photothermal capabilities that make them versatile tools for targeting specific cells for destruction through multimodal therapeutic interventions.

Our research has pursued three distinct engineering approaches: the use of phonon sensitizers, manipulation of host phonon modes, and co-doping with lanthanide elements. We have incorporated an Nd³⁺ phonon sensitizer into various host lattices to progressively increase phonon modes. This deliberate engineering reduces photon emission while significantly boosting phonon generation. Moreover, the introduction of Sm³⁺ as a co-dopant, with energy transfer states closely aligned with the system, leads to additional non-radiative pathways. This co-doping enhances the performance of PA imaging, especially in host lattices with F and VO₄. By combining these three different approaches, we have

achieved a high degree of sensitivity and specificity *in vivo* using lanthanide-doped nanocrystals.

The synergistic combination of techniques has not only advanced the field of PA imaging, but also paved the way for NIR-PAMDI. This advanced imaging modality enables simultaneous visualization of multiple targets with distinct lanthanide dopants and provides insights into their spatial distribution and relative concentrations within biological tissues.

Methods

Instrumentation

Transmission electron (TEM) measurements were performed with a JEOL-JEM 2010F field emission transmission electron microscope operated at an acceleration voltage of 200 kV. Raman spectral measurements were obtained with a HORIBA Jobin Yvon Modular Raman microscope equipped with two laser sources (514 nm and 633 nm). The spectrum was scanned from 500 cm^{-1} to 4000 cm^{-1} using a 50x microscope objective. FTIR spectra were obtained from Bruker Alpha FTIR spectroscopy in KBr pellets.

Chemicals

All chemicals were of analytical grade and were used without further purification. Rare earth acetates, yttrium (III) acetate hydrate ($\text{Y}(\text{CH}_3\text{CO}_2)_3$; 99.9%), and neodymium (III) acetate hydrate ($\text{Nd}(\text{CH}_3\text{CO}_2)_3$; 99.9%) were purchased from Sigma Aldrich. Rare-earth chlorides, yttrium (III) chloride (>99.99%), neodymium (III) chloride (99.9%), and samarium (III) chloride (>99.99 + %) were purchased from Sigma Aldrich. The following reagents were also obtained from Sigma Aldrich: sodium orthovanadate (Na_3VO_4 ; 99.98%) oleic acid (90%), 1-Octadecene (90%), ammonium fluoride (NH_4F ; >98%), sodium hydroxide (NaOH ; >98%), HCL (37%), and polyvinylpyrrolidone ($M_w = 55,000$).

Synthesis of Nd-doped NaYF_4 nanocrystals

The procedure for synthesizing lanthanide-doped NaYF_4 nanocrystals was adopted from Wang et al. with some modifications³⁷. In a 50-mL three-neck round-bottomed flask, 7 mL of 1-octadecene (ODE) and 3 mL of oleic acid (OA) were mixed with 2 mL of 0.2 M $\text{Ln}(\text{CH}_3\text{COO})_3$ ($\text{Ln} = \text{Y}^{3+}, \text{Nd}^{3+}$) in aqueous solution. The mixture was stirred at 150 °C for 90 min to yield lanthanide oleate complexes in organic media. The light-yellow solution was cooled to 50 °C and then a mixture of NaOH methanol solution (0.5 M, 2 mL) and NH_4F methanol solution (0.4 M, 4 mL) was added. For core-shell synthesis, the pre-made nanocrystals in cyclohexane were added to the reaction flask directly before the addition of the $\text{NaOH-NH}_4\text{F}$ mixture. After 30 min, the reaction mixture was brought to 105 °C for 10 min, degassed, and purged with argon at least three times. The reaction mixture was then heated to 290 °C for 2 h under a nitrogen flow. The final product was then purified three times and re-dispersed in 4 mL of cyclohexane.

Synthesis of ligand-free NaYF_4 nanocrystals

The as-synthesized NaYF_4 nanocrystals were transferred to the aqueous phase by acid-induced ligand removal. First, 1 mL of 0.4 mmol nanocrystals was added to 1 mL of ethanol and centrifuged at 16,500 rpm for 10 min. Then the nanocrystals were re-suspended in 0.5 mL of ethanol, 1 mL of 0.2 M HCl was added, and the mixture was washed with water at 16,500 rpm for 20 min. This process is repeated three times. Finally, the nanocrystals were resuspended in 2 mL of deionized water.

Synthesis of polyvinylpyrrolidone (PVP)-coated NaYF_4 nanocrystals

The synthesized ligand-free NaYF_4 nanocrystals (1 ml) were added to a 2-mL of 5% (w per v) PVP solution, and the resultant mixture was stirred overnight. The NaYF_4 @PVP nanocrystals were then separated via centrifugation at 16,500 rpm and washed two times with water. Finally, the nanocrystals were resuspended in 1 mL of deionized water.

General strategy for the synthesis of Nd^{3+} -doped YVO_4 and $\text{Y}(\text{OH})_3$ nanocrystals

The synthesis procedure for nanocrystals with the varying host was adapted from Wang et al. with some modification³⁷. The particle synthesis was inspired by the idea of using adequate ligands to stabilize salt compounds at the nanoscale. A 2 mL solution of 0.1 M of LnCl_3 ($\text{Ln} = \text{Nd}^{3+}, \text{Y}^{3+}, \text{Dy}^{3+}, \text{Sm}^{3+}$) was mixed with 1 mL of 5% (w per v) polyvinylpyrrolidone (PVP) at 60 °C. Subsequently, 2 mL of 0.095 M of Na_3VO_4 or 0.285 M NaOH was added into the mixture and stirred for 10 min before being transferred into a 20 mL Teflon-lined autoclave. The resultant mixture was heated at 180 °C for 2 h. The obtained nanocrystals were collected by centrifugation and purified with DI water before re-suspension in 4 mL of either water or 0.9% saline solution.

First-principles calculations of phonon density of states

Optimization and electronic structure calculations were performed using the VASP^{38–40} code with projector-augmented-wave (PAW) pseudopotentials and Perdew-Burke-Ernzerhof (PBE) exchange and correlation functionals. The plane-wave energy cutoff was set to 350 eV, and the k-mesh was chosen as a $4 \times 4 \times 4$ grid for structural minimization. The energy convergence criterion for electronic iteration in VASP was set to 10^{-8} eV. Structures were relaxed until the force on each ion was less than 10^{-5} eV \AA^{-1} . A $4 \times 4 \times 4$ supercell was used for the calculations. The phonon dispersion and density of states were calculated utilizing the finite displacement method implemented in the Phonopy package⁴¹.

Absorbance measurements of Lanthanide nanocrystals for photothermal (PT), photoacoustic (PA), and photoluminescence (PL) studies

Colloidal solutions of the three host lattice nanocrystals showed significant baseline elevation due to scattering in standard line-of-sight UV-VIS absorption measurements. As a result, the height of the absorbance peak after baseline correction was used to represent the real absorption ratio. For PL measurements, a cuvette containing 1.5 mL of the colloidal solution was excited in an Edinburgh FL-1000 fluorescence spectrophotometer (Edinburgh Instruments) equipped with an 803 nm CW diode laser source (MDL-N-808; Changchun New Industries Tech Co Ltd; FWHM, 4 nm). The resulting photoluminescence peak intensities were then corrected for their relative absorption over the excitation wavelength range.

In vitro PA studies

PA spectra of the samples were recorded using an MSOT EIP 10 (iThera Medical), a commercial PA imaging system. The bandwidth of the piezoelectric ultrasound transducer ranged from 200 kHz to around 7 MHz. Polyethylene tubes holding sample solutions were 4 cm long. The tube wall was 0.25 mm thick, and the outside diameter was 1.50 mm. For imaging, 30 μL of each sample solution was positioned at the transducer's focal point in a water tank. A pulsed laser with a pulse width of 5–10 ns and wavelengths ranging from 700 nm to 900 nm at 1 nm intervals was used to excite the sample, with a pulse energy of ~80 mJ per pulse. PA spectra were obtained after averaging 30 times with a laser pulse rate of 10 Hz. Ultrapure water was used as the reference for each run to analyze the PA signals on the same basis.

Contrast images demonstrating wavelength selectivity were obtained by imaging processing in Image J. PA images of difference were calculated using the following equation:

$$I = I_{\lambda_{\text{max}}} - I_{\lambda_{\text{max}} - x \text{ nm}}, \quad (1)$$

where $I_{\lambda_{\text{max}}}$ is the PA image obtained at the maximum PA wavelength (λ_{max}), and $I_{\lambda_{\text{max}} - x \text{ nm}}$ is the PA image x nm away from the maximum PA wavelength (λ_{max}).

In vivo PAT system

A lab-made optical parametric oscillator (OPO) laser, pumped by an Nd:YAG laser at a 100 Hz pulse repetition rate, was used to output specific wavelengths of light for PA excitation. The laser beam was first homogenized by an optical diffuser (EDC-5, RPC Photonics) and then illuminated the sample from above. PA signals were detected by a full-ring piezoelectric ultrasonic transducer array (Imasonic) with a 10-cm diameter, a 5-MHz central frequency, more than 90% one-way bandwidth, and 512 elements. Each element (20-mm height, 0.61-mm pitch, and 0.1-mm inter-element spacing) was cylindrically focused to produce an axial focal distance of 45 mm (acoustic NA, 0.22). The combined foci of all 512 elements formed an approximately uniform imaging region with a 20-mm diameter and 1-mm thickness. In this region, the in-plane spatial resolution was $\sim 150 \mu\text{m}$. A lab-made 512-channel preamplifier (26 dB gain) was directly connected to the ultrasonic transducer array housing with a minimized connection cable length to reduce cable noise. The pre-amplified PA signals were digitized using a 512-channel data acquisition system (four SonixDAQs, Ultrasonix Medical ULC; 128 channels each; 40-MHz sampling rate; 12-bit dynamic range) with programmable amplification up to 51 dB. The data acquisition time for each frame was 50 μs . Each laser pulse yielded a widefield image, and the frame rate was 10 Hz, currently limited by the laser repetition rate. The digitized radio frequency data were first stored in the onboard buffer and then transferred to a computer. Digitized raw data were fed into a universal back-projection algorithm at half the speed of sound for image reconstruction^{42–44}.

Linear unmixing

We separated the phonon-enhanced signals of lanthanide nanocrystals from the background by using linear spectral unmixing. The total absorption coefficient $\mu_a(\lambda_i)$ is

$$\mu_a(\lambda_i) = \sum_j \varepsilon_j(\lambda_i) [j], \quad (2)$$

where $\varepsilon_j(\lambda_i)$ is the known molar extinction coefficient of absorber j at wavelength λ_i , and $[j]$ is the concentration of the respective chromophore. The amplitude of the reconstructed PA signal is proportional to the absorption coefficient at that location. Therefore, the relative concentrations can be computed by finding the least squares solution for each position \mathbf{r} for

$$\mathbf{P}_0 = \mathbf{kMN}, \quad (3)$$

where $\mathbf{P}_0 = (p_0(\mathbf{r}, \lambda_i))$, $\mathbf{M} = (\varepsilon_j(\lambda_i))$, $\mathbf{N} = ([j])$, and k is a proportionality constant that depends on the imaging parameters and local fluence.

For in vitro studies (Fig. 4), we used four wavelengths: 865 nm, 871 nm, 878 nm, and 884 nm to effectively unmix the PA signals of nanocrystals from blood, including Nd(OH)₃, NdVO₄, NaNdF₄, and hemoglobin by solving Eq. (4).

$$\begin{bmatrix} p_0(\mathbf{r}, 865\text{nm}) \\ p_0(\mathbf{r}, 871\text{nm}) \\ p_0(\mathbf{r}, 878\text{nm}) \\ p_0(\mathbf{r}, 884\text{nm}) \end{bmatrix} = \begin{bmatrix} \varepsilon_{\text{Nd(OH)}_3}(865\text{nm}) & \varepsilon_{\text{NdVO}_4}(865\text{nm}) & \varepsilon_{\text{NaNdF}_4}(865\text{nm}) & \varepsilon_{\text{Hb}}(865\text{nm}) \\ \varepsilon_{\text{Nd(OH)}_3}(871\text{nm}) & \varepsilon_{\text{NdVO}_4}(871\text{nm}) & \varepsilon_{\text{NaNdF}_4}(871\text{nm}) & \varepsilon_{\text{Hb}}(871\text{nm}) \\ \varepsilon_{\text{Nd(OH)}_3}(878\text{nm}) & \varepsilon_{\text{NdVO}_4}(878\text{nm}) & \varepsilon_{\text{NaNdF}_4}(878\text{nm}) & \varepsilon_{\text{Hb}}(878\text{nm}) \\ \varepsilon_{\text{Nd(OH)}_3}(884\text{nm}) & \varepsilon_{\text{NdVO}_4}(884\text{nm}) & \varepsilon_{\text{NaNdF}_4}(884\text{nm}) & \varepsilon_{\text{Hb}}(884\text{nm}) \end{bmatrix} \begin{bmatrix} [\text{Nd(OH)}_3] \\ [\text{NdVO}_4] \\ [\text{NaNdF}_4] \\ [\text{Hb}] \end{bmatrix} \quad (4)$$

Preparation of animals

Adult 2- to 3-month-old female nude mice (Hsd:ATHymic Nude-Fox1NU, Harlan; body weight, ~ 20 – 30 g) were used for all in vivo experiments. All experimental procedures were carried out in conformity with laboratory

animal protocols approved by the Institutional Animal Care and Use Committee of California Institute of Technology (IA20-1737). Throughout the experiment, mice were anesthetized with 1.5% vaporized isoflurane. Prior to brain imaging, the hair on the mouse head was removed with depilatory cream, and the scalp was then cleaned with alcohol swabs. During in vivo imaging, the mouse was secured to a lab-made imaging platform and the cortical surface of the brain was aligned flat with the focal plane of the transducer array. During imaging, 100 μL of Nd(OH)₃ at a concentration of 60 mg mL⁻¹ was injected via the tail vein. Throughout the experiment, the animal body temperature was regulated at 38 °C.

In vitro toxicity studies of Ln-nanocrystals and their constituent ions

A typical MTS cell viability assay using U-87MG cells containing both tetrazolium compound [3-(4,5-dimethylthiazol-2-yl)-5-(3-carboxymethoxyphenyl)-2-(4-sulfophenyl)-2H-tetrazolium, inner salt; MTS] and an electron coupling reagent (phenazine ethosulfate; PES) was performed to examine the in vitro cytotoxicity of the as-synthesized lanthanide nanocrystals. Briefly, U-87MG cells were seeded in a 96-well plate (5000 cells per well) and incubated overnight in a humidified atmosphere of 5% CO₂ before ensuring that the cells adhered to the wells. After incubation, different concentrations (0.0313, 0.0625, 0.125, 0.250, 0.5, and 1.0 mg mL⁻¹) of lanthanide-doped nanocrystals were added to each well of the 96-well plate, followed by incubation for another 24 h. After incubation, the medium in each well was removed, and 100 μL of fresh medium and 20 μL of MTS solution (CellTiter 96[®]A_{queous}, Promega) were added and incubated for another 3 h. Subsequently, absorbance was monitored using a microplate reader (Varioskan Flash Multimode Reader, Thermo Scientific) at a wavelength of 490 nm. Cytotoxicity was expressed as the percentage of viable cells compared to untreated control cells.

Reporting summary

Further information on research design is available in the Nature Portfolio Reporting Summary linked to this article.

Data availability

The data that supports the findings of this study are available from the corresponding authors upon reasonable requests.

Received: 4 January 2024; Accepted: 7 August 2024;

Published online: 21 August 2024

References

- Bell, A. G. *On the production and reproduction of sound by light* (S.N, 1880).
- Kim, C., Favazza, C. & Wang, L. H. V. In Vivo Photoacoustic Tomography of Chemicals: High-Resolution Functional and Molecular Optical Imaging at New Depths. *Chem. Rev.* **110**, 2756–2782 (2010).
- Wang, L. H. V. & Yao, J. J. A practical guide to photoacoustic tomography in the life sciences. *Nat. Methods* **13**, 627–638 (2016).
- Weber, J., Beard, P. C. & Bohndiek, S. E. Contrast agents for molecular photoacoustic imaging. *Nat. Methods* **13**, 639–650 (2016).
- Kothapalli, S. R. et al. Simultaneous transrectal ultrasound and photoacoustic human prostate imaging. *Sci. Transl. Med.* **11**, eaav2169 (2019).
- Kim, C., Song, K. H., Gao, F. & Wang, L. H. V. Sentinel Lymph Nodes and Lymphatic Vessels: Noninvasive Dual-Modality in Vivo Mapping by Using Indocyanine Green in Rats-Volumetric Spectroscopic Photoacoustic Imaging and Planar Fluorescence Imaging. *Radiology* **255**, 442–450 (2010).
- Pu, K. et al. Semiconducting polymer nanoparticles as photoacoustic molecular imaging probes in living mice. *Nat. Nanotechnol.* **9**, 233 (2014).

8. De La Zerda, A. et al. Carbon nanotubes as photoacoustic molecular imaging agents in living mice. *Nat. Nanotechnol.* **3**, 557 (2008).
9. Zhang, H. F., Maslov, K., Stoica, G. & Wang, L. H. V. Functional photoacoustic microscopy for high-resolution and noninvasive in vivo imaging. *Nat. Biotechnol.* **24**, 848–851 (2006).
10. Li, L. et al. Small near-infrared photochromic protein for photoacoustic multi-contrast imaging and detection of protein interactions in vivo. *Nat. Commun.* **9**, 2734 (2018).
11. Yao, J. J. et al. Multiscale photoacoustic tomography using reversibly switchable bacterial phytochrome as a near-infrared photochromic probe. *Nat. Methods* **13**, 67–73 (2016).
12. Wang, L. D., Maslov, K. & Wang, L. H. V. Single-cell label-free photoacoustic flowoxigraphy in vivo. *P Natl Acad. Sci. USA* **110**, 5759–5764 (2013).
13. Hai, P. F. et al. Label-free high-throughput photoacoustic tomography of suspected circulating melanoma tumor cells in patients in vivo. *J. Biomed. Opt.* **25**, 1–17 (2020).
14. Wang, X. D. et al. Noninvasive laser-induced photoacoustic tomography for structural and functional in vivo imaging of the brain. *Nat. Biotechnol.* **21**, 803–806 (2003).
15. Ntziachristos, V., Ripoll, J., Wang, L. V. & Weissleder, R. Looking and listening to light: the evolution of whole-body photonic imaging. *Nat. Biotechnol.* **23**, 313 (2005).
16. Wang, L. V. & Hu, S. Photoacoustic Tomography: In Vivo Imaging from Organelles to Organs. *Science* **335**, 1458–1462 (2012).
17. Wahsner, J., Gale, E. M., Rodriguez-Rodriguez, A. & Caravan, P. Chemistry of MRI Contrast Agents: Current Challenges and New Frontiers. *Chem. Rev.* **119**, 957–1057 (2019).
18. Lusic, H. & Grinstaff, M. W. X-ray-Computed Tomography Contrast Agents. *Chem. Rev.* **113**, 1641–1666 (2013).
19. Deshpande, N., Needles, A. & Willmann, J. K. Molecular ultrasound imaging: current status and future directions. *Clin. Radio.* **65**, 567–581 (2010).
20. Zhao, Z. X., Swartzchick, C. B. & Chan, J. Targeted contrast agents and activatable probes for photoacoustic imaging of cancer. *Chem. Soc. Rev.* **51**, 829–868 (2022).
21. Liu, C. et al. Reversibly Photoswitching Upconversion Nanoparticles for Super-Sensitive Photoacoustic Molecular Imaging. *Angew. Chem. Int. Ed. Engl.* **61**, e202116802 (2022).
22. Maji, S. K. et al. Upconversion nanoparticles as a contrast agent for photoacoustic imaging in live mice. *Adv. Mater.* **26**, 5633–5638 (2014).
23. Sheng, Y., Liao, L.-D., Thakor, N. & Tan, M. Rare-Earth Doped Particles as Dual-Modality Contrast Agent for Minimally-Invasive Luminescence and Dual-Wavelength Photoacoustic Imaging. *Sci. Rep.* **4**, 6562 (2014).
24. Sheng, Y. et al. Size and Shell Effects on the Photoacoustic and Luminescence Properties of Dual Modal Rare-Earth Doped Nanoparticles for Infrared Photoacoustic Imaging. *ACS Biomater. Sci. Eng.* **2**, 809–817 (2016).
25. Zhan, Q. Q. et al. Using 915 nm Laser Excited Tm³⁺/Er³⁺/Ho³⁺–Doped NaYbF₄ Upconversion Nanoparticles for in Vitro and Deeper in Vivo Bioimaging without Overheating Irradiation. *ACS Nano* **5**, 3744–3757 (2011).
26. Zou, W. Q., Visser, C., Maduro, J. A., Pshenichnikov, M. S. & Hummelen, J. C. Broadband dye-sensitized upconversion of near-infrared light. *Nat. Photonics* **6**, 560–564 (2012).
27. Shen, J. et al. Engineering the Upconversion Nanoparticle Excitation Wavelength: Cascade Sensitization of Tri-doped Upconversion Colloidal Nanoparticles at 800 nm. *Adv. Opt. Mater.* **1**, 644–650 (2013).
28. Xie, X. J. et al. Mechanistic Investigation of Photon Upconversion in Nd³⁺-Sensitized Core-Shell Nanoparticles. *J. Am. Chem. Soc.* **135**, 12608–12611 (2013).
29. Danielmeyer, H. G., Blätte, M. & Balmer, P. Fluorescence quenching in Nd:YAG. *Appl. Phys.* **1**, 269–274 (1973).
30. Bednarkiewicz, A., Wawrzynczyk, D., Nyk, M. & Strek, W. Optically stimulated heating using Nd³⁺ doped NaYF₄ colloidal near infrared nanophosphors. *Appl. Phys. B* **103**, 847–852 (2010).
31. Wang, F. & Liu, X. G. Recent advances in the chemistry of lanthanide-doped upconversion nanocrystals. *Chem. Soc. Rev.* **38**, 976–989 (2009).
32. Riseberg, L. A. & Weber, M. J. in *Progress in Optics* 14 (ed Wolf, E.) 89–159 (Elsevier, 1977).
33. Blasse, G. & Grabmaier, B. C. in *Luminescent Materials* (eds G. Blasse & B. C. Grabmaier) 71–77 (Springer Berlin Heidelberg, 1994).
34. Chen, Y.-S. et al. Silica-Coated Gold Nanorods as Photoacoustic Signal Nanoamplifiers. *Nano Lett.* **11**, 348–354 (2011).
35. Zhen, X., Feng, X., Xie, C., Zheng, Y. & Pu, K. Surface engineering of semiconducting polymer nanoparticles for amplified photoacoustic imaging. *Biomaterials* **127**, 97–106 (2017).
36. Atkins, P. W. & Friedman, R. *Molecular quantum mechanics*, 5th edn, (Oxford University Press, 2011).
37. Wang, F., Deng, R. & Liu, X. Preparation of core-shell NaGdF₄ nanoparticles doped with luminescent lanthanide ions to be used as upconversion-based probes. *Nat. Protoc.* **9**, 1634–1644 (2014).
38. Kresse, G. & Joubert, D. From ultrasoft pseudopotentials to the projector augmented-wave method. *Phys. Rev.* **59**, 1758 (1999).
39. Kresse, G. & Hafner, J. Ab initio molecular dynamics for liquid metals. *Phys. Rev. B* **47**, 558 (1993).
40. Kresse, G. & Hafner, J. Ab initio molecular-dynamics simulation of the liquid-metal. *Phys. Rev. B* **49**, 14251 (1994).
41. Togo, A., Chaput, L. & Tadano, T. & Isao Tanaka, Implementation strategies in phonopy and phono3py, *J. Phys. Condens. Matter* **35**, 353001–351 (2023).
42. Li, L. et al. Single-impulse panoramic photoacoustic computed tomography of small-animal whole-body dynamics at high spatiotemporal resolution. *Nat. Biomed. Eng.* **1**, 0071 (2017).
43. Wu, Z. G. et al. A microrobotic system guided by photoacoustic computed tomography for targeted navigation in intestines in vivo. *Sci. Robot* **4**, eaax0613 (2019).
44. Lee, C. et al. Dual-color photoacoustic lymph node imaging using nanoformulated naphthalocyanines. *Biomaterials* **73**, 142–148 (2015).

Acknowledgements

We are very grateful to Renzhe Bi and Xiuting Li for their assistance in the initial stages of testing our nanocrystals in PA experiments. We also like to thank Melgious Ang for his assistance in conducting cellular toxicity studies on the nanocrystals. We also like to express our gratitude to Ding Ding for provided technical insights and guidance on experimental interpretation. This work is supported by National Research Foundation, Prime Minister's Office, Singapore under its Competitive Research Program (Award No. NRF-CRP23-2019-0002) and under its NRF Investigatorship Programme (Award No. NRF-NRFI05-2019-0003), the RIE2025 Manufacturing, Trade and Connectivity (MTC) Programmatic Fund (Award No. M21J9b0085), and National Institutes of Health, United States, grants U01 NS099717 (BRAIN Initiative) and R01 EB028277A, the internal fund F10000205 from Rice University, the Basic Science Center Program for Ordered Energy Conversion of the National Natural Science Foundation of China (No. 51888103), National Natural Science Foundation of China (51606192) and the CAS Pioneer Hundred Talents Program. Partial supports by A*STAR, Singapore, RIE2020 Advanced Manufacturing and Engineering (AME) Programmatic Fund (Grant No. A20G9b0135) are acknowledged.

Author contributions

K.Y.L., L.S.L., J.F., Y.Y.G., designed the project. L.V.W. and X.L. supervised the project. K.Y.L., J.F., Y.Y.G. synthesized the nanocrystals and performed characterization experiments. L.S.L., S.D., Y.Z., W.H.L. performed in vitro and in vivo PA measurements. K.L. and Jie Liu synthesized organic dye. P.M. performed in vivo tumor photothermal therapy. M.Y. and H.Z. carried out the first principles phonon calculations for the different host materials

and extracted the six high energy optical phonon modes in the OH host. Z.M. and W.G. conducted temperature dependent photoluminescence measurements. M.F. and T.C.S. conducted absorbance measurements with an integrating sphere. L.L., P.M., G.F., W.G., T.C.S., Jun Lin, B.L., and K.Y. provided technical guidance. K.Y.L., L.S.L., J.F., and Y.Y.G. were primarily responsible for data collection and results analysis and prepared the figures and Supplementary Information. K.Y.L., L.S.L., J.F., Y.Y.G., L.V.W., and X.L. wrote the manuscript. All authors contributed to the discussion and editing of the manuscript.

Competing interests

The authors declare the following competing interests: L.V.W. has financial interests in Microphotoacoustics, Inc., CalPACT, LLC, and Union Photoacoustic Technologies, Ltd., which did not support this work. L.S.L. has a financial interest in BLOCH Quantum Imaging Solutions, although they did not support this work. The other authors declare no competing interests.

Additional information

Supplementary information The online version contains supplementary material available at <https://doi.org/10.1038/s43246-024-00605-1>.

Correspondence and requests for materials should be addressed to Lihong V. Wang or Xiaogang Liu.

Peer review information *Communications materials* thanks Jeesu Kim and the other, anonymous, reviewer(s) for their contribution to the peer review of this work. Primary Handling Editors: Jet-Sing Lee. A peer review file is available.

Reprints and permissions information is available at <http://www.nature.com/reprints>

Publisher's note Springer Nature remains neutral with regard to jurisdictional claims in published maps and institutional affiliations.

Open Access This article is licensed under a Creative Commons Attribution 4.0 International License, which permits use, sharing, adaptation, distribution and reproduction in any medium or format, as long as you give appropriate credit to the original author(s) and the source, provide a link to the Creative Commons licence, and indicate if changes were made. The images or other third party material in this article are included in the article's Creative Commons licence, unless indicated otherwise in a credit line to the material. If material is not included in the article's Creative Commons licence and your intended use is not permitted by statutory regulation or exceeds the permitted use, you will need to obtain permission directly from the copyright holder. To view a copy of this licence, visit <http://creativecommons.org/licenses/by/4.0/>.

© The Author(s) 2024